Paramagnetic Iron-Doped Hydroxyapatite Nanoparticles with Improved Metal Sorption Properties. A Bioorganic Substrates-Mediated Synthesis

Paramagnetic Iron-Doped Hydroxyapatite Nanoparticles with Improved Metal Sorption Properties. A Bio-Organic Substrates-Mediated Synthesis.

ACS APPLIED MATERIALS & INTERFACES 6, 3937-3946

Paramagnetic Iron-Doped Hydroxyapatite Nanoparticles with Improved Metal Sorption Properties. A Bio-Organic Substrates-Mediated Synthesis.

D. Fabio Mercado,[a] Giuliana Magnacca,[b] Mery Malandrino,[b] Aldo Rubert,[a] Enzo Montoneri,[b] Luisella Celi,[c] Alessandra Bianco Prevot,[b] and Mónica C. Gonzalez*[a]

[a] *Instituto de Investigaciones Fisicoquímicas Teóricas y Aplicadas (INIFTA), CCT-La Plata-CONICET, Universidad Nacional de La Plata, La Plata, Argentina.*

[b]*Dipartimento di Chimica, Università di Torino, Via Giuria 7, Torino, Italy.*

[c]*Dipartimento di Scienze Agrarie, Forestali e Alimentari, Università di Torino, Via Leonardo Da Vinci, 44 – Grugliasco, Torino, Italy.*

• *Corresponding author E-mail*: gonzalez@inifta.unlp.edu.ar

Abstract

This paper describes the synthesis of paramegnetic iron-containing hydroxyapatite nanoparticles and their increased Cu^{2+} sorbent capacity when using Ca^{2+} complexes of soluble bio-organic substrates from urban wastes as synthesis precursors. A thorough characterization of the particles by TEM, XRD, FTIR spectroscopy, specific surface area, TGA, XPS, and DLS, indicates that loss of crystallinity, a higher specific area, an increased surface oxygen content, and formation of surface iron phases strongly enhance Cu^{2+} adsorption capacity of hydroxyapatite-based materials. However, the major effect of the surface and morphologycal modifications is the size diminution of the aggregates formed in aqueous solutions leading to an increased effective surface available for Cu^{2+} adsorption. Maximum sorption values of 550 - 850 mg Cu^{2+} per gram of particles suspended in an aqueous solution at pH 7 were determined; almost 10 times the maximum values observed for hydroxyapatite nanoparticles suspensions under the same conditions.

Keywords: Magnetic Nanomaterials; Cu^{2+} Sorption; Effective surface; Bio-Organic Substrates; Surface chemistry.

Introduction

Hydroxyapatite (Ap), $Ca_{10}(PO_4)_6(OH)_2$, the main component of the bone tissue of vertebrates, is one of the most promising sorbent materials for removing actinides and heavy metals from wastewaters and soils. Apatites of the most different origins, such as cow bone charcoal,[1] nano-Ap (nAp),[2] waste oyster shells,[3] and bacteria,[4] were used for the removal of heavy metals. Ap is an ideal material for long-term sequestration in aqueous reservoirs because of its chemical stability across a wide range of geological conditions,[5] high biocompatibility, strong ability to fix actinides and heavy metals,[6] and maximum metal ion sorption capacity

at pH 6 – 7.[2]

Humates are also widely applied to clean up toxic waste sites. Formation of humates is based on the ability of carboxyl and hydroxyl groups of humic and/or fulvic acids to bind metal cations. In particular, Ca^{2+} are effective precipitators of humates and provide a route for the transfer of trace metals from the solution to the solid phase.[7] Moreover, formation of stable, water-soluble phosphate-Ca^{2+}-humic complexes[8] were reported. Urban bio-wastes (UBW) have been reported to contain soluble humic-like substances known as bioorganic substances (SBO) which show promise as chemical auxiliaries for a number of technological applications in the chemical industry and in environmental remediation.[9] UBW-SBO are mixtures of substances with molecular weights in the range $(1–3)\times10^5$ Da, formed by long aliphatic C chains substituted by aromatic rings and COOH, NCO, C=O, PhOH, O-alkyl, O-aryl, OCO, OMe, and alkyl amines functional groups. Therefore, the use of UBW-SBO as templates in the synthesis of Ap materials may be expected to affect Ap morphology and surface chemistry, as observed for organic matrix-mediated fabrication of nanostructured hydroxyapatite biocomposites.[10]

Nanomaterials showing high specific surface area and tunable surface chemistry were suggested to offer significant improvement as metal adsorbents.[11] In particular, magnetite-incorporated hydroxyapatite composites attract much attention as a magnetic functional material for developing adsorbents and catalysts since they could be easily removed by application of a magnetic field.[12] However, to date, the metal adsorption capacity of these materials was not assessed.

In this context, in the present comunication we describe the synthesis of Ap-based magnetic nanoparticles and their increased metal sorption capacity when synthetized using Ca^{2+} complexes of UBW-SBO as synthesis precursors.

Experimental

Reactants

Calcium chloride 95 wt%, phosphoric acid 85%, $FeCl_2.4H_2O$ > 99 %wt, $FeCl_3.6H_2O$ 97 wt%, were supplied by Sigma Aldrich and used without further purification. Deionized water was Milli-Q purified (18.2 MΩcm and 6 ppb TOC). When required, pH was stabilized to 7.0 with 4-(2-hydroxyethyl)piperazine-1-ethanesulfonic acid, sodium salt (HEPES-Na) and nitric acid.

The biorganic substances herein used where available from a pilot plant from Studio Chiono&Associati in Rivarolo Canavese, Italy. The fraction of soluble biorganic substances used, namely CVT230, was extracted from home gardening and park trimming residues aerated for 230 days for aerobic microbiological treatment; the resulting biomass was digested with an alkali solution at 65 ^oC for several hours and the remaining supernatant filtered by an UF membrane operating with tangential flow to yield a retentate with 5-10 % dry matter content. The concentrated retentate (CVT230) was finally dried at 60 °C. CVT230 was 72.1% solid residue, and composed of 38.25 ± 0.09 % w/w C and 4.01 ± 0.03 % w/w N. Among the important mineral residues are: 256 ppm Zn, 202 ppm Cu, 92 ppm Ni, 85 ppm Pb, 19 ppm Cr, and minor amounts of Si, Fe, and Ca. CVT230 carbon fractions are: 37% alifatic, 20 % aromatic, 14% alkoxy, 12 % carboxilic, and 7%

are in an α position to amines.[13] SBO were reported to be non-toxic to *Vibrio Fischeri*, activated sludge bacteria, *Daphnia magna,* and *Pseudokirchneriella subcapitata*. Their reported biological to chemical oxygen demand ratio, BOD:COD < 0.1, indicates an extremely low biodegradability.

Addition of excess Ca^{2+} to SBO aqueous solutions of pH 11 leads to the formation of insoluble SBO-Ca^{2+} products which became solubilized on decreasing the pH to 5. The observed behaviour resembles that of humic and fulvic acids complexation with Ca^{2+}ions.[14]

Synthesis of hydroxyapatite magnetic nanoparticles

A modification of literature methods was used for the synthesis of hydroxyapatite nanoparticles, nAp.[15] Briefly, a suspension of $Ca(OH)_2$ (5 g in 40 ml H_2O) was stirred and heated to 80 ^oC. A phosphoric acid solution (4.44 g in 60 ml of H_2O) was added drop-wise into the calcium hydroxide suspension over a period of 2 h under constant heating and stirring, to obtain a suspension of nAp. The precipitate was separated from the mother liquor by centrifugation, washed several times with deionized water and dried at 80 ^oC.

The previous process was adapted for the synthesis of Fe-containing hydroxyapatite nanoparticles, denoted as Fe-nAp. A $FeCl_2.4H_2O$ (1.27 g), $FeCl_3.6H_2O$ (1.79 g) phosphoric acid (4.44 g in 60 ml of H_2O) solution was added drop-wise into a $Ca(OH)_2$ suspension (5 g in 40 ml H_2O) over a period of 2 h under constant stirring and heating at 80 ^oC. The total amounts of iron to calcium ions were adjusted to obtain an analytical molar ratio of Fe/Ca = 0.2. The reaction products were kept in suspension with constant stirring for 24 h at room temperature. The precipitate was separated from the mother liquor either by centrifugation or by means of a laboratory magnet bar of c.a. 2000 G, then washed several times with deionized water and dried at 80 ^oC.

For the synthesis of SBO-templated iron-containing hydroxyapatite nanoparticles, either 20, 200, or 1000 mg of SBO were dissolved in a $Ca(OH)_2$ suspension (5 g in 40 ml H_2O) and the resulting suspension stirred for 2 hours at 80 ^oC. A $FeCl_2.4H_2O$ (1.27 g), $FeCl_3.6H_2O$ (1.79 g) phosphoric acid (4.44 g in 60 ml of H_2O) solution was then added drop-wise into the $Ca(OH)_2$ – SBO suspension over a period of 2 h under constant stirring and heating at 80 ^oC. The reaction mixture was kept in suspension with constant stirring for 24 h at room temperature. The precipitate was separated from the mother liquor by centrifugation and by means of a laboratory magnet bar, and then washed several times with deionized water until no SBO was observed in the washing liquors by, both, UV-vis spectroscopy and total organic carbon assays. All the particles were dried at 80^{o}C. The particles were named 0.05SBO-Fe-nAp, 0.5SBO-Fe-nAp, and 2.5SBO-Fe-nAp, according to the SBO/Ca w/w ratio used in the synthesis. When requiered, 2.5SBO-Fe-nAp powders were further calcined at 600 ^oC for 3 hours. Calcined particles are therefore named 2.5SBO-Fe-nAp-cal.

Particle characterization

The crystalline phase content of samples was assessed by X-ray Diffraction (XRD) by using a PW3040/60 X'Pert PRO MPD X-ray diffractometer from PANalytical, in Bragg-Brentano geometry, equipped with the high power ceramic tube PW3373/10 LFF source with Cu anode. The qualitative phase analysis was performed with the EVA software package and compared to the ICDD- PDF-2- database. The effect of Fe

and SBO treatment on nAp crystallites domain size, D_v, were evaluated. A lower limit value of D_v was calculated employing the Scherrer equation relating the size of sub-micrometre particles in a solid to the broadening of diffraction pattern main peaks[17] and considering k = 0.9 as the shape factor and $\lambda = 0.154056$ nm as the wave length of the X-rays for Cu Kα1 radiation.

High resolution transmission electron microscopy (HRTEM) studies were carried out on a JEOL JEM 3010UHR (300 kV) TEM fitted with a single crystal LaB_6 filament. Samples were dry deposited on Cu "holey" carbon grids (200 mesh).

The thermal behaviour of the powders was studied by thermal gravimetric analysis (TGA) using a Q600 TA Instruments. The program used a nitrogen environment and involved a one minute initial temperature of 50 ^oC, followed by a 20 ^oC /min ramp up to 800 ^oC and maintained at this temperature for 10 minutes. For some samples, an oxygen enviroment was also used.

The functional groups present in the prepared nanoparticles were identified by their IR spectrum obtained with a Bruker IFS28 spectrophotometer equipped with a Globar source and a DTGS detector working at 128 scans with 4 cm^{-1} resolution in the overall range 4000–400 cm^{-1}. Samples were prepared by pressing a grounded mixture of 1% of the particles powder with 99% dry KBr at a load of 5 tons.

Nitrogen gas-volumetric adsorption experiments for specific surface area determinations (BET model) were performed at 77 K by means of a ASAP2020 by Micromeritics model. Before each measurement, samples were outgassed overnight at 80 °C at a residual pressure of about 10^{-2} mbar to guarantee a good cleaning of the sample surface.

The X-ray photoelectron spectroscopy (XPS) spectra were obtained under UHV with a XR50 Specs GmbH spectrometer using Mg K(α) as the excitation source and a PHOIBOS 100 half sphere electron energy analyzer. A two-point calibration of the energy scale was performed using sputtered cleaned gold (Au 4f7/2, binding energy (BE) 84.00 eV) and copper (Cu 2p3/2, BE: 932.67 eV) samples. Internal calibration to correct for surface charging was performed with the C 1s peak at BE= 284.6 eV due to adventitious carbon. High resolution XPS spectra were taken to get a better insight into the chemical environment of the different atoms. A Shirley-type background from each spectrum was used to remove the effect of the extrinsic structure loss and the espectrum resolved by Gaussian-Lorentzian fitting, keeping $\chi 2$ values to their minimum values.

The electrophoretic mobility was measured by Laser Doppler Velocimetry- Photon Correlation Spectroscopy using a DELSA 440 spectrometer (Beckman Coulter Electronics, Hialeah, FL) equipped with a 5 mW HeNe laser (632.8 nm).

The magnetic characteristics of the particles was assessed using a Lakeshore 7403 vibrating sample magnetometer. Magnetization of dried samples was performed at room temperature up to a maximum field of 1.9T.

Metal determinations were performed with a Perkin Elmer Optima 7000 DV Model inductively coupled plasma atomic emission spectrometer (ICP-AES). The instrument is equipped with a Echelle monochromator, a cyclonic spray chamber, and a PTFE Mira Mist nebulizer. The instrumental conditions

were: plasma power 1.3 kW; sample aspiration rate 1.2 mL/min; argon cooling flow 1.5 L/min; argon sampling flow 0.6 L/min. The overall P:Ca:Fe ratio of the synthetized particles was also measured by ICP after acid digestion of the particles.

Metal adsorption experiments

Adsorption studies were conducted in batch experiments. Variable ml-aliquots of a $Cu(NO_3)_2$ stock solution of 1000.0 mg L^{-1} were mixed with 5 ml of a 100 ppm solution of either nAp, Fe-nAp, 0.05SBO-Fe-nAp, 0.5SBO-Fe-nAp, 2.5SBO-Fe-nAp, or 2.5SBO-Fe-nAp-cal, and further diluted to a final volume of 25 mL with a solution of 4-(2-hydroxyethyl) piperazine-1-ethanesulfonic acid sodium salt (HEPES-Na) of pH 7 and 0.01 M ionic strength. The highest [Cu^{2+}] used was limited by Cu^{2+} solubility.[18]

The suspensions were shaken at room temperature (25 ± 2°C) for several hours until equilibration was observed. Preliminary experiments showed that equilibration takes place already after one hour. The supernatant and solid residues were separated by centrifugation at 4,000 rpm for 10 min. The Cu concentration in the supernatant solutions was determined by ICP-AES. The amount of adsorbed Cu was calculated according to $x/m = v\times(C_o-C_e)/m$, where x/m (mg g^{-1}) is the weight in mg of Cu^{2+} ions adsorbed per g of particles, C_o and C_e (mg.L^{-1}) stand for the initial and equilibrium Cu^{2+} concentrations in solution, respectively, v (L) is the solution volume used in the experiment and *m* (g) is the mass of particles used. Data were expressed as the mean of three replicates.

Results and Discussion

A flow chart of the pathways followed for the synthesis of the different particles is described in Scheme 1.

Scheme 1: Flow chart of the synthesis pathways used for obtaining the different particles. "x" denotes the SBO/Ca w/w analytical ratio after mixing.

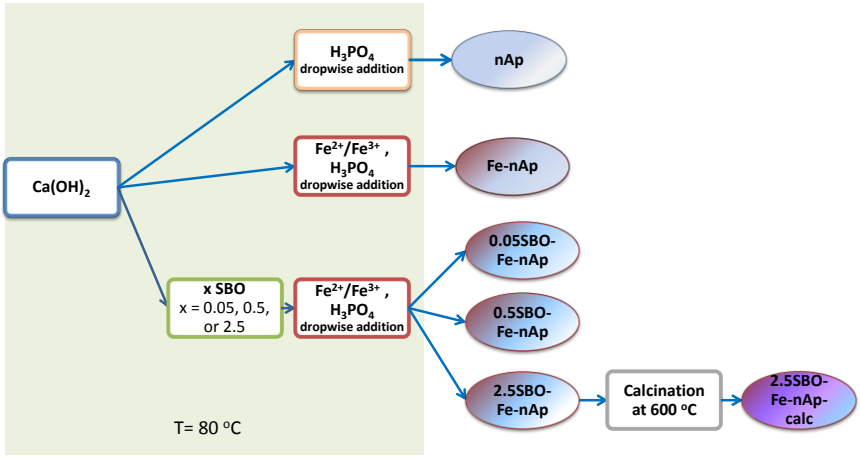

Particle characterization

The effect of SBO and Fe on the physical and chemical properties of nAp was studied and compared with untreated nAp. Figure 1 shows comparative HRTEM micrographs of the prepared powders. Due to

substantial agglomeration it is not possible to obtain a statistic analysis of the particles size. However, the micrographs show cylindrical, 100 - 150 nm length, crystalline nAp particles, as indicated by the presence of interference fringe patterns observable at high resolution. Fe-nAp particles show somewhat shorter (50 – 100 nm) acicular shapes of irregular contour. The latter observation is in line with the reported effect on the morphology of rod-like nanometer size crystalline nAp which became elongated and the crystallinity slightly lowered upon addition of Fe(III) ions,[19] *vide infra*. Inhibition of hydroxyapatite *c*-axis and promotion of the *a*-axis by added Fe(II) during a co-precipitation synthesis was also reported.[20]

The use of 2.5 w(SBO)/w(Ca) as template in the synthesis of the particles leads to an even more heterogeneous sample of irregular acicular particles. Calcination of 2.5SBO-Fe-nAp leads to an increased size heterogeneity with a predominant population of enlarged particles. In all the micrographs relative to Fe-containing samples, it is possible to observe the presence of globular lumps characterized by higher optical density assignable to iron-containing domains of nanometric size (< 10 nm), as also reported for Fe-containing particles obtained by similar synthetic procedures.[16,17] The lumps are distributed quite homogeneously in the materials, indicating that the synthesis in the presence of Fe^{2+}/Fe^{3+} salts brought about a good dispersion of iron-containing phases on Ap-based materials. This characteristic seems to be enhanced in the SBO patterned particles.

The XRD diffractograms of nAp-based materials are shown in Figure 2. Hydroxyapatite XRD patterns are observed in all the prepared powders with no significant shifting of peak positions, thus suggesting that Fe^{2+}/ Fe^{3+} incorporation did not greatly modify the hydroxyapatite structure. A marked broadening increase of the XRD peaks of Fe-nAp, and particularly of 2.5SBO-Fe-nAp and 2.5SBO-Fe-nAp-cal powders, strongly indicates an important reduction in the crytalline structure of the particles. In addition, these samples exhibit more intense diffraction peaks at $2\theta = 35.5$, as well as peaks of lower intensity at $2\theta = 30.2$ and 62.5, characteristic of magnetite and maghemite structures (depicted in figure 2). Despite the presence of magnetite and maghemite crystalline phases is being supported, they could not be unambigously differentiated, since their XRD diffraction spectrum mainly differ in the relative intensity of the peaks. In fact, the obtained XRD data closely resembles those reported for Fe-containing hydroxyapatites from different synthetic methods.[15, 16, 21]

Figure 1: HRTEM micrographs. Circles show iron-containing domains.

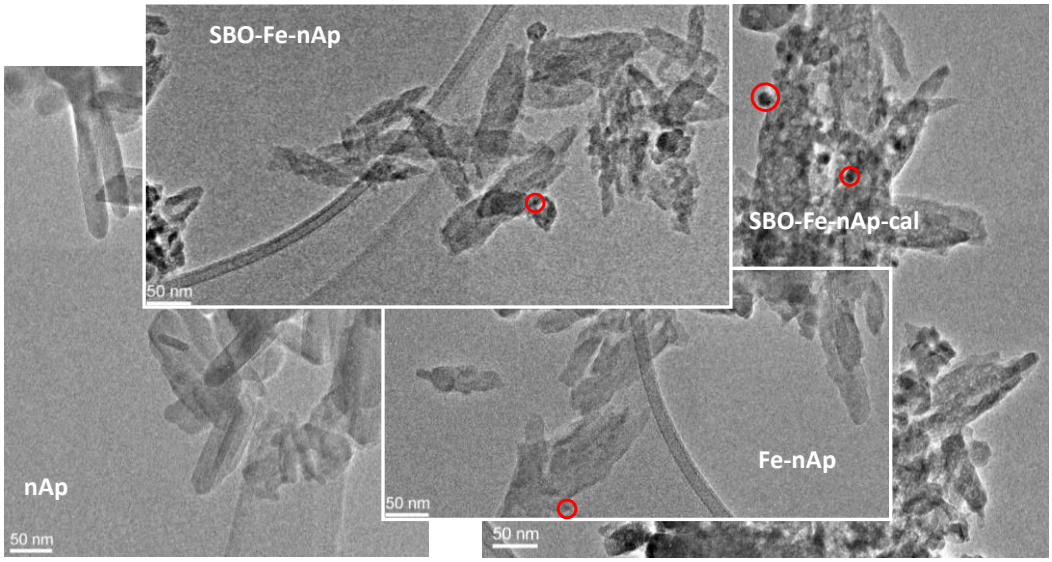

Figure 2: X-ray diffractograms of (from top to down) nAp, Fe-nAp, 2.5SBO-Fe-nAp, and 2.5SBO-Fe-nAp-cal. Bars stand for hydroxyapatite (black), maghemite (cyan), and magnetite (pink) principal reference patterns. Astericks indicate the 2θ = 35.5 diffraction peak.

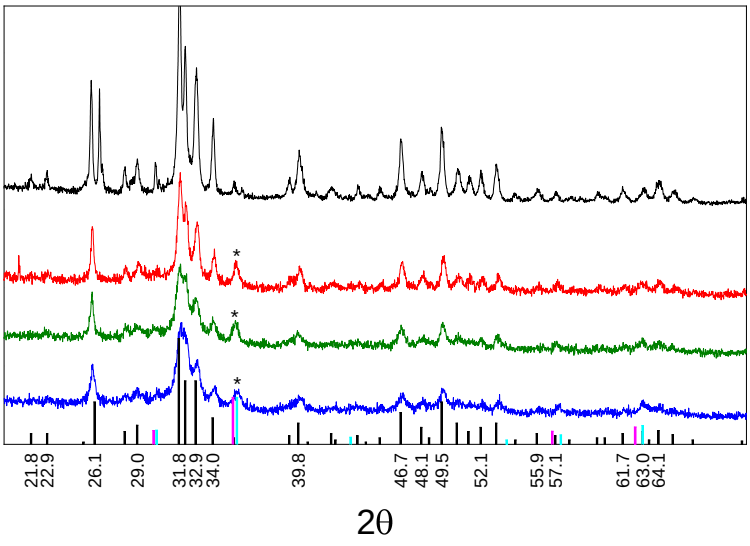

The FTIR spectra of the particles are shown in Figure 3. nAp spectrum shows the fundamental vibration modes of PO_4 groups of the apatitic structure at about 470, 560, 610, 960 and 1030-1100 cm^{-1}.[22] Moreover, the band at 870 and 1460 cm^{-1} attributed to residual carbonate from the synthesis process are also observed. The broad bands in the regions 1640 and 3430 cm^{-1} correspond to δH-O-H bands and νOH signals due to HOH bands of lattice and physisorbed water molecules. The IR spectrum of Fe-nAp shows mainly peaks atributed to nAp. The characteristic peaks due to iron oxides in the 600 – 400 cm^{-1} range[23] may be occluded by those of nAp due to the low amount of iron present in the samples. The 2.5SBO-Fe-nAp spectrum shown in Figure 3B evidences nAp signals overimposed to those of SBO (also shown in the figure). The intense

bands at 3430 and 1649 cm^{-1} indicates the presence of HO groups of phenols, alcohols and carboxyl groups, and of C=O bonds of carboxyl and carbonyl moieties, respectively. On the other hand, the FTIR absorption peaks of 2.5SBO-Fe-nAp-cal may be assigned mainly to those of nAp, thus indicating that 3 hours calcination at 600 ^{o}C of 2.5SBO-Fe-nAp powders is effective in eliminating SBO residues. nAp spectrum also shows the sharp hydroxyl bands at 632 and 3572 cm^{-1}, typical of nAp with a high degree of crystallinity. The absence of these peaks in the spectra of all the other particles suggests that the powders show poor crytallinity, in agreement with XRD data also supporting a decreased hydroxyapatite cristallinity upon Fe addition and use of SBO as organic template.

Figure 3: FTIR spectra (from down to top): (A) nAp, Fe-nAp, and 2.5SBO-Fe-nAp-cal. (B) SBO and 2.5SBO-Fe-nAp.

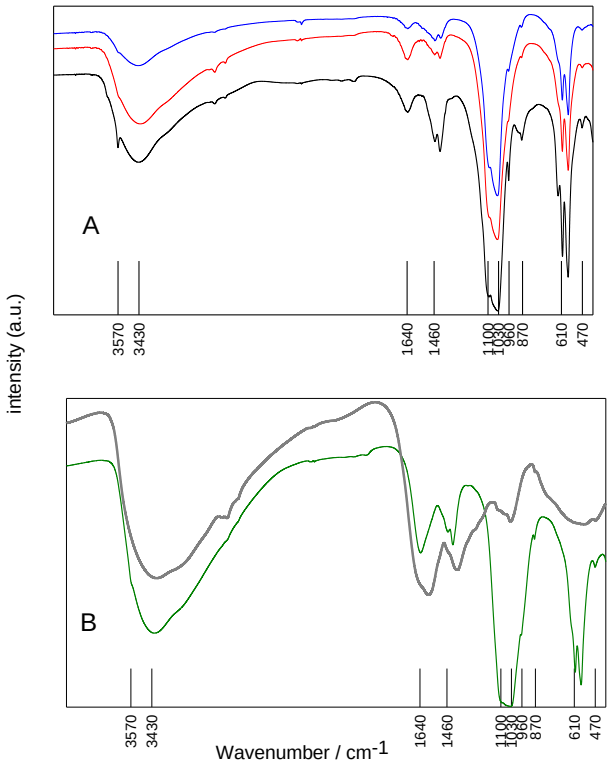

The TGA curves (see Figure 4) obtained in a N_2 environment in the temperature range from 80 to 800 ^{o}C for Ap-based materials yield information on the adsorbed substrates, as decomposition of the Ap structure is expected at temperatures over 900 ^{o}C.[22] The 5.9 % total mass loss of nAp is attributed to adsorbed water (T ≤ 100 ^{o}C), dehydration of hydroxides (380 -500 ^{o}C), and elimination of surface carbonate-like groups (500 - 800 ^{o}C), in good agreement with literature reports for nano-sized Ap powders.[22] Fe-nAp shows an 8% total mass loss between 80 and 800 ^{o}C attributed to adsorbed water, dehydration of Fe hydroxides (380 -500 ^{o}C), and elimination of surface carbonate-like groups. On the other hand, 2.5SBO-Fe-nAp powder shows a 14 %

total mass loss suggesting an important contribution of SBO pyrolysis (curve not shown), in agreement with the fact that only a 4 % weight loss is observed for the same particles calcined for three-hours at 600 ^{o}C. The latter observations are in agreement with the FTIR spectra indicating the presence of SBO in 2.5SBO-Fe-nAp, and a complete elimination of the organic template in the calcined powders. An estimation of the particles carbon content may be obtained from the mass loss in the temperature range from 200 to 380 ^{o}C observed in TGA curves performed in O_2 environment. Approximately 5% mass content due to SBO is estimated for 2.5SBO-Fe-nAp. TGA curves of 0.5SBO-Fe-nAp and 0.05SBO-Fe-nAp performed in the presence of O_2 agree, within the experimental error, with that of Fe-nAp, indicating that no significant amounts (< 1%) of organic matter is present in the materials.

Figure 4: TGA performed in a N_2 atmosphere, curves (A) nAp, (B) Fe-nAp, and (C) 2.5SBO-Fe-nAp-cal. TGA performed in an O_2 atmosphere, curves (D) 0.05SBO-Fe-nAp, (E) 0.5SBO-Fe-nAp, and (F) 2.5SBO-Fe-nAp. Corresponding derivative curves are shown in S1.

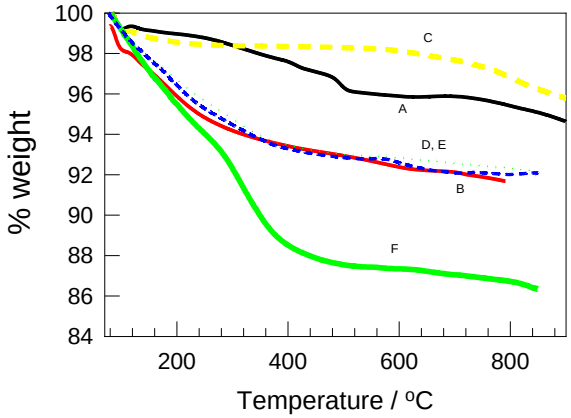

Table 1 depicts the specific surface area of the synthetized powders as determined by BET model and the relative crystallites domain size as estimated by Scherrer equation using the XRD data. Crystalline nAp shows the lowest surface area while almost a twofold increase is observed for Fe-nAp, and a further 15% increase is observed for 2.5SBO-Fe-nAp. Calcination of the latter reduces the surface area by 15%. The BET isotherms show hysteresis mainly at high P/P^0 values related to N_2 condensation inside inter-particle macropores of ca. 100 nm (see S2). Crystallite domain sizes decrease in the trend nAp < Fe-nAp < 2.5SBO-Fe-nAp while a further increase is observed for 2.5SBO-Fe-nAp-cal. All together, the results suggest a reduced crystallite domain size with increasing specific surface area and particle size diminution. The increase of specific surface area besides crystallinity diminution is also reported for nanoparticulated apatite.[24]

Table 1: Specific surface area as obtained from BET isotherms, lower limit size as estimated by the Scherrer equation, surface stoichiometric ratio obtained by XPS analysis, % C from TGA experiments, electrophoretic mobility (μ) in the pH range from 6.5 to 7, bulk Ca and Fe percentages, and Fe to Ca molar ratio in the particle bulk.

Particle Type	Specific surface area /m^2g^{-1}	crystallite domain size/nm	Surface composition	% w/w SBO	μ (mS/cm)	% Ca w/w	% Fe w/w	Fe/Ca
							bulk	
nAp	34	30–50	$Ca_1P_{0.7}O_{3.1}Fe_0$	0	+0.95	38.4	< 0.02	0
Fe- nAp	64	20-40	$Ca_1P_{0.9}O_{4.6}Fe_{0.14}$	0	-1.8	28.4	7.8	0.2
0.05SBO-Fe-nAp	68	----	----	< 1	-1.5	31.2	7.4	0.17
0.5SBO-Fe-nAp	70	----	$Ca_1P_{0.7}O_{3.7}Fe_{0.09}$	< 1	-1.6	29.0	6.9	0.17
2.5SBO-Fe-nAp	71	10-30	$Ca_1P_{0.75}O_{3.7}Fe_{0.09}$	~5	-1.8	28.3	6.6	0.17
2.5SBO-Fe-nAp-cal	64	20-60	$Ca_1P_{0.8}O_{3.3}Fe_{0.06}$	0	-----	30.9	7.2	0.17

The average hydrodynamic particle size distribution determined by DLS measurements, shown in Figure 5, indicates that the particles hydrodynamic sizes are several fold-times higher than the sizes observed in TEM micrographs. Thus, important aggregation in aqueous solutions at pH 7 and 0.01 M ionic strength takes place. The amount of SBO used as template in the particles synthesis strongly influences aggregation, as smaller hydrodynamic sizes are observed for increasing SBO concentrations. Calcination of 2.5SBO-Fe-nAp particles increases the aggregates size, in line with the population of larger particles depicted in the corresponding HRTEM micrographs (*vide supra*). Aggregate sizes in the range of 100 nm are observed for 2.5SBO-Fe-nAp particles, and interparticle macroporosity of almost the same size is evidenced by N_2 gas-volumetric adsorption, thus indicating that macropores formed in the solid state do not have real significance in aqueous suspensions of the particles.

Figure 5: Hydrodynamic particle size distribution as obtained by DLS for nAp (A), Fe-nAp (B), 2.5SBO-Fe-nAp (C), 2.5SBO-Fe-NA-cal (D), 0.5SBO-Fe-nAp (*inset*, E), and 0.05SBO-Fe-nAp (*inset*, F).

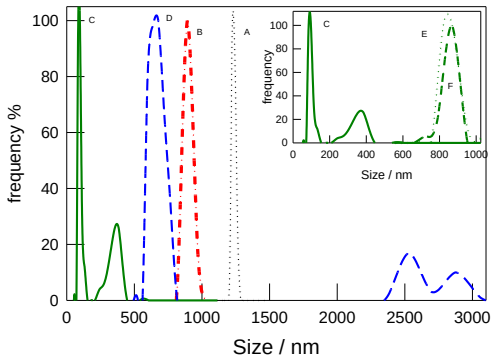

The electrophoretic mobility of the particles obtained in the pH range from 6.5 to 7 are depicted in Table 1. nAp and Fe-nAp values of +0.95 and -1.8 mS/cm, respectively, indicate that the incorporation of 20% Fe on the hydroxyapatite particles brings about an increased surface charge density and a predominance of negative surface charges. Moreover, SBO-patterned particles show electrophoretic mobilities similar to those observed for Fe-nAp. The contrast between the similar mobilities of these particles with their different

aggregates size strongly suggests an increased surface hydrophylicity in SBO-patterned particles due to the presence of uncharged surface groups which strongly stabilize the aqueous suspensions of the particles.

The XPS survey spectra of the particles (see S4) depict the main lines for Ca, O, P, and Fe (except for nAp). Beside these peaks, a C(1s) "adventitious carbon" peak was observed which was used for binding energy correction due to charging effects by setting it to 284.6 eV. Carbonate-type carbon, incorporated during synthesis, was also observed. All powders show the Ca2p1/2 (350.8eV) and Ca2p3/2 (347.4 eV) lines, and the P2s line at 191 eV due to calcium phosphate in apatite (see S5). On the other hand, analysis of Fe2p3/2 peaks is more controversial. The use of broad peak shapes has proved useful for the identification of pure compounds but of lesser use for the identification of mixtures due to the spectral overlap of most Fe(III) compounds which show similar binding energies but varying peak shapes and satellite intensities.[25] In fact, such analysis leads to a peak at about 710.5 eV with a satellite displaced 4 eV and a second broad peak at about 712.5 eV with no satellite contribution unless overlapped to the Fe2p1/2 portion of the spectrum. These peaks did not match the reported data of neither pure Fe oxides[26] nor of phosphated iron.[27] Therefore, Fe2p3/2 peaks for all the iron-containing samples herein synthesized were modelled using a combination of ferrous and ferric multiplet patterns for the lower and higher energy portion of the spectrum, respectively,[25, 28] as shown in Figure 6 for Fe-nAp. Fe2p3/2 signal adjustment was performed assuming a Shirley type baseline and using the lowest number of peaks allowed with about 1.7 eV FWHM, except for the peak attributed to Fe II satellite which was left free. All samples show contributing peaks at 709.5, 710.9, 712.2, 713.4, 714.9 eV, and Fe^{2+} satellite peak shifted by 4.8- 5 eV, in line with the patterns reported for Fe(II)-PO_4 surface oxidized to Fe(III)-OH.[28] Moreover, no metallic component can be observed in the spectrum indicating its absence in the surface layer. The observed satellite peak at c.a. 719 eV, may be assigned to the contribution of iron oxides.[26, 29] Observed Fe2p3/2 and Fe2p1/2 signals separations, ΔE (BE 2p3/2 −BE 2p1/2), of about 13.0–13.3 eV are in agreement with reported data for Fe oxides and salts.[26] Therefore, the XPS data points to a complex mixture of Fe^{2+} / Fe^{3+} phosphates and oxides on the particles surface.

Deconvolution of the O1s peak of n-Ap shows the main contribution of a band at 531.8 eV (96%) and a minor contribution at 532.8 eV. According to literature reports, these peaks may be assigned to oxygen atoms in phosphates and hydroxyls, and to adsorbed water, respectively, in agreement with reported data for hydroxyapatite.[27] On the other hand, O1s peaks of Fe-containing particles are best modelled when the contribution of a third peak at c.a. 530.1 eV characteristic of O atoms in iron oxide environments is considered,[26] as depicted in Figure 6 *inset* and S5. Peak contributions of 22 % and 13% were observed for Fe-nAp and 2.5SBO-Fe-nAp-cal, respectively, while contributions of c.a. 5% where observed for 0.5SBO-Fe-nAp and 2.5SBO-Fe-nAp. The latter observations are in line with the larger peak area of Fe2p3/2 multiplets of BE > 711 eV observed for Fe-nAp and 2.5SBO-Fe-nAp-cal, normally identified with Fe^{3+} ions.

Figure 6: XPS Fe2p3/2 and Fe2p1/2 signals (full line) for 2.5SBO-Fe-nAp and contributing peaks (dashed lines). *Inset:* O1s signals (full line) and contributing species (dashed lines).

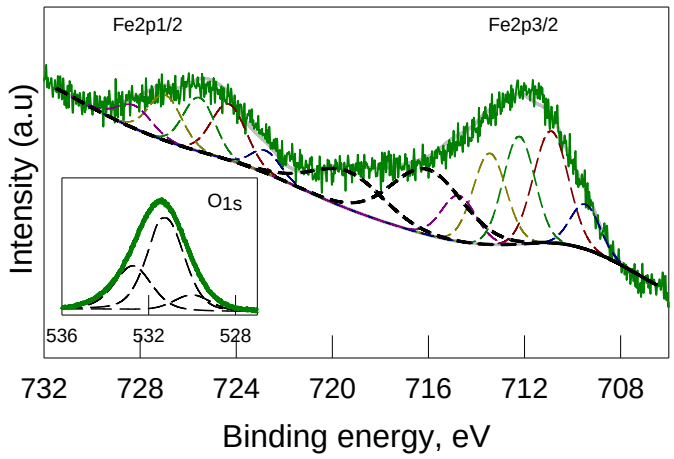

Considering the experimental sensitivity factors relative to the different elements, a surface Ca:P:O stoichiometric ratio was determined for each particle type as depicted in Table 1. The P/Ca ratio for nAp is somewhat higher than the expected theoretical $Ca(PO_4)_{0.6}O_{0.2}$ stoichiometric ratio but close to the values reported in the literature for several hydroxyapatite materials and attributed to the presence of surface acid phosphates.[29] On the other hand, the O/P ratio is, within the experimental error, in line with the expected value for hydroxyapatite. Fe-nAp shows higher P/Ca and O/Ca ratios than nAp. All together, the data seems to indicate that surface iron increases phosphate content due to the formation of Fe(II)-phosphates while surface Fe^{3+} seems to lead to the formation of iron oxides. In fact, Fe(III)-substituted hydroxyapatite nanoparticles were reported to show an increased surface hydrophilicity as a consequence of the formation of surface Fe-OH groups, though the number of original Ca(II) atoms was reduced.[19]

On the other hand, lower Fe/Ca surface ratios were observed when SBO was used as template in the particle synthesis. 0.5SBO-Fe-nAp and 2.5SBO-Fe-nAp show P/Ca ratios similar to those of nAp, though the respective O/Ca ratios are significantly higher, thus suggesting the presence of surface OH groups. Upon calcination, 2.5SBO-Fe-nAp show a decreased content in surface oxygen and iron.

Hysteretic M-H curves of Fe-nAp and 2.5SBO-Fe-nAp at 300K (see S3) exhibit a superparamagnetic behavior with zero coercivity and zero remanence on the magnetization curves. For both particles, the saturation magnetization was of 4 emu/g of particles, in line with reported values for Fe-nAp nanopowders.[15, 16] Considering a 7% w/w iron content in the particles (see Table 1), the saturation magnetization per gram of iron is 57 emu/g Fe, half the value expected for magnetite nanoparticles.[30] Therefore, formation of significant amounts of iron compounds not contributing to the overall paramagnetism is supported.

The described results clearly indicate that introduction of Fe^{3+} / Fe^{2+} ions and the use of SBO-Ca^{2+} complexes as templates during hydroxyapatite synthesis leads to a diminution in the apatite crystalline structure, a negatively charged surface, and an increased surface hydrophilicity. Formation of magnetite and/or maghemite is observed by XRD. However, iron oxides formation is not the only fate of iron. The loss of crystallinty of the apatite structure might be a consequence of Ca^{2+} exchange by Fe^{2+}/ Fe^{3+} ions. In fact, XPS analysis clearly indicates the presence of surface Fe^{2+} phosphates salts and oxidized Fe^{3+}. Formation of

surface FeO and OH groups is suggested from the O2s peak analysis. A comparison between Fe:Ca contents in the particles volume and at the surface, see Table 1, indicates that Fe ions are preferentially incorporated in the particles core.

Metal adsorption capacity

Figure 7 shows the measured Cu^{2+} adsorption isotherms. The one-adsorption site Langmuir model, eq. (1), fits the isotherms of Cu^{2+} adsorption on nAp, Fe-nAp, 0.05SBO-Fe-nAp, and 0.5SBO-Fe-nAp with regression coefficients $r^2 > 0.95$. The obtained fitting parameters are depicted in Table 2. The affinity coefficient of Cu^{2+} adsorption, k_L, shows the trend nAp ≈ Fe-nAp > 0.05SBO-Fe-nAp ≈ 0.5SBO-Fe-nAp while the maximum number of sites b increases in the order nAp < Fe-nAp < 0.05SBO-Fe-nAp < 0.5SBO-Fe-nAp. On the other hand, adsorption on 2.5SBO-Fe-nAp and 2.5SBO-Fe-nAp-cal particles were better fitted by the Freundlich model, eq. (2). This experimental isotherm has been interpreted to arise from an heterogeneous surface showing a distribution of different adsorption sites, where $1/n \leq 1$ is an experimentally determined exponent and k_F the Freundlich constant. However, within the experimental error, obtained values of n are close to 1, thus suggesting the applicability of the Langmuir isotherm under the condition $1 >> k_L \times C_e$ and $k_F = k_L \times b$. In fact, the maximum Cu^{2+} absorption could not be reached for these particles due to the limited Cu^{2+} solubility.[18] Taking $k_L \times b$ = 90 mg g^{-1} for 2.5SBO-Fe-nAp and considering $k_L \approx 0.11$ for SBO-templated particles (*vide supra*), results $b \approx 850 \pm 400$ mg g^{-1}.

$$x/m = \frac{k_L \times b \times C_e}{1 + k_L \times C_e} \qquad eq.(1)$$

$$x/m = k_F \times C_e^{1/n} \qquad eq.(2)$$

Figure 7: Cu^{2+} adsorption isotherms at 25 °C. Main figure: Fe-nAp (●), 0.05SBO-Fe-nAp (∇), and 0.5SBO-Fe-nAp (■). *Inset left*: 2.5SBO-Fe-nAp (Δ), and 2.5SBO-Fe-nAp-cal (⬢). *Inset right*: nAp (○). The solid lines and dashed lines stand to the fitting of the data to eq.(1) and (2), respectively.

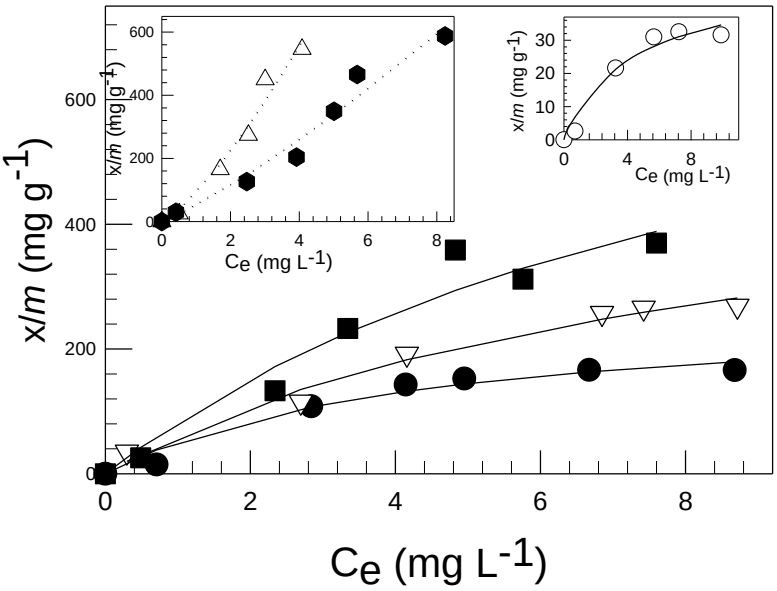

Table 2: Fitting parameter values of the Langmuir and Freundlich models. Error bars are denoted in parentheses.

Particle	eq.	b /mg g^{-1}	k_L	1/n	k_F / mg g^{-1}	r
nAp	1	50(25)	0.22(0.1)			0.967
Fe-nAp	1	265(60)	0.24(0.02)			0.969
0.05SBO-Fe-npA	1	550(200)	0.12(0.04)			0.978
0.5SBO-Fe-nAp	1	850(400)	0.10(0.07)			0.953
2.5SBO-Fe-nAp	2			1.3(0.2)	90(22)	0.974
2.5SBO-Fe-nAp-cal	2			1.2(0.2)	50(15)	0.970

Isolation of the Cu^{2+}-adsorbed nAp, Fe-nAp, and 0.5SBO-Fe-nAp and further resuspension in an aqueous solution of pH 7, show 0.2, 0.1, and 0.02 % Cu^{2+} leaching after two hours, respectively. Thus indicating that $Cu^{2+}$is strongly chemisorbed at pH 7.

The obtained value of b for nAp is in line with that reported for Cu^{2+} adsorption on commercial nanohydroxyapatite at pH 7.2 (64.8 mg g^{-1}), though the reported[2] k_L = 0.80 is almost 4 times higher than that found here. An even number of regularly spaced, positively charged, calcium ions and negatively charged oxygen groups on the surface of crystalline Ap support metal cation retention due to ion exchange and/or coordination with P-sites and surface HO. Moreover, Cu^{2+} precipitation with free PO_4^{3-} ions as a consequence of the high Ap solubility at pH 5 is also reported.[31] In our experiments, the amounts of calcium and iron ion concentrations measured in solution during the Cu^{2+} adsorption experiments are *c.a.* 17 and 0.5

μg/g NP, respectively, for all the particles, independently of the adsorbed amount of Cu^{2+} ions. Therefore, Cu^{2+} exchange for Ca^{2+} and Fe^{2+} in the hydroxyapatite structure seems not to significantly contribute to Cu^{2+} adsorption under our experimental conditions.

Moreover, the observed increase in the specific surface area of Fe-nAp and SBO-Fe-nAp containing particles seems not to be the cause of the increased Cu^{2+} adsorption of these materials (*vide infra*), as normalization of the adsorption isotherms by the specific surface area of the materials does not modify the observed trend.

Reported Cu^{2+} maximum adsorption capacities for different magnetite composites are of the order of 1.9 for aqueous suspensions of pH 5.5,[32] 56.71 for magnetite-immobilized chitin,[33] and 140-150 mg/g for magnetite-immobilized *pseudomonas putida* 5X cells at pH 7.[32] These values are below those observed for the materials herein synthesized. On the other hand, Cu^{2+} ions have been reported to readily form non-labile complexes with fulvic acids and dissolved natural organic matter, DOM,[34] as amino groups, phenolic hydroxyls and adjacent aromatic carboxylates provide lone pairs of electrons for chelating Cu^{2+} ions. The reported total number of binding sites range from 1 to 100 μM mgC^{-1} depending on pH, ionic strength, and the DOM origin and concentration. A rough estimation of the adsorption sites provided by SBO may be obtained if it is considered that 5% mass of 2.5SBO-Fe-nAp is due to SBO organic residues, from which 38.5 % in weight is due to C atoms. Therefore, taking the maximum amount of 100μM sites mgC^{-1}, ~122 mg g^{-1} Cu^{2+} ions would be adsorbed by the organic matter, well below the obtained values (see Table 2). Consequently, the increased Cu^{2+} adsorption capacity observed for SBO-patterned particles cannot be assigned solely to surface-trapped SBO, neither to the small magnetite domains observed on the particles surface. These observations are further supported by the significant Cu^{2+} adsorption capacity still observed for 2.5SBO-Fe-nAp-cal despite the elimination of all C-containing residues due to calcination.

As discussed above, the main differences observed between nAp and Fe-containing apatites involve a reduction in the crystallinity of hydroxyapatite domains, a reduced Ca^{2+} content, and the formation of surface phosphated iron and magnetite/maghemite phases. An increased O-content is also observed at the surface of all SBO-Fe-nAp materials. Such surface and structural modifications might support an increased adsorption efficiency of the iron-containing hydroxyapatite materials due to Cu^{2+}complexation with surface PO_4 and OH groups. It results striking though, that despite both 0.5SBO-Fe-nAp and 2.5SBO-Fe-nAp showing similar surface composition, except for the small C content of the latter, Cu^{2+} adsorption ability of 2.5SBO-Fe-nAp is significantly higher. We suggest therefore, that the smaller aggregates formed by 2.5SBO-Fe-nAp in aqueous suspensions makes the particles surface more available for Cu^{2+} adsorption. In fact, strong electrostatic interactions might prevent Cu^{2+} ions to approach the binding sites of the particles surface within the aggregates. Surface area measurements of dry materials do not necessarily represent the effective surface area of suspended particles in aqueous solution because of the particles agglomeration in suspension.[35, 36]

A rough estimation of the effective surface area may be obtained if it is assumed that Cu^{2+} is mainly adsorbed at the agglomerates surface, and taking the agglomerates hydrodynamic radius distribution

measured by DLS and the density value of hydroxyapatite (3.156 g/cm^3)[37] for all the particles. Normalization of the isotherms shown in Figure 6 by the estimated effective agglomerate area (1.55, 2.1, 2.2, 2.3, 6.5, and 2.8 m^2g^{-1} for nAp, Fe-nAp, 0.05SBO-Fe-nAp, 0.5SBO-Fe-nAp, 2.5SBO-Fe-nAp, and 2.5SBO-Fe-nAp-cal, respectively) yields adsorption isotherms (see Figure 8) which may be classified in two main groups: nAp and Fe-containing apatites. Iron-containing particles, all depicting similar k_L values, show improved adsorption capacity with respect to pure nAp, in line with their described surface characteristics, *vide supra*. Differences among the adsorption isotherms of the iron-containing particles are mainly observed at high Cu^{2+} loadings, probably due to Cu^{2+} adsorption on the particles surface facing the interior of the agglomerates at higher concentrations, a situation not considered in the simplified estimation of the effective surface area.

Figure 8: Cu^{2+} adsorption isotherms at 25 ^oC normalized by the effective area (see text). nAp (○), Fe-nAp (●), 0.05SBO-Fe-nAp (▽), 0.5SBO-Fe-nAp (■), 2.5SBO-Fe-nAp (△), and 2.5SBO-Fe-nAp-cal (⬢).

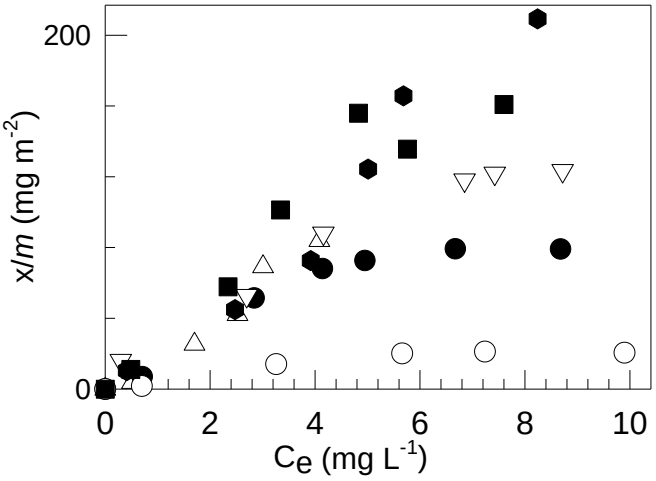

Conclusions

The present results strongly indicate that hydroxyapatite nanoparticles doped with iron and synthetized using SBO as template, show significant changes in the particles morphology and surface chemistry. Among the observed effects are: a reduction in the crystallinity of hydroxyapatite domains, elongated and smaller particles with higher specific surface area, reduced Ca^{2+} content, formation of surface phosphated iron and iron oxides, increased oxygen content at the surface, and an overall negative surface charge at pH 7.0. Moreover, formation of magnetite oxide seems responsible for the particle paramagnetism. Such surface and structural modifications support the formation of stable homogeneous aqueous suspensions of the particles,

which show a reduction in the size of the agglomerates when increasing the SBO content in the synthesis procedure.

A significant improvement in the Cu^{2+} adsorption capacity was observed upon iron-doping of the hydroxyapatite particles and, particularly, for the SBO-templated particles. Such improvement is correlated with a negatively-charged surface and the presence of phosphate and Fe-OH surface groups. However, a second important effect appears to be the agglomerates size, as agglomeration seems to severely reduce the effective surface available for adsorption in aqueous suspensions.

The materials herein synthetized are a potential, self-sustaining, environmentaly friendly, and efficient material for Cu^{2+} remediation in aqueous effluents. Future work involves metal sorption selectivity studies and metal desorption conditions for particle reuse.

Aknowledgement

D.F.M. thanks Consejo Nacional de Investigaciones Científicas y Técnicas (CONICET, Argentina) for a graduate studentship. M.C.G. is a research member of CONICET. The work was performed partly with funds of the Ministero Italiano delle Politiche Agricole within the Agrienergia project and by the grant PIP 112-200801-00356 from CONICET, Argentina. Financial support for academic interchange by the European Union (IRSES-GA-2010-269128, EnvironBOS) is acknowledged. The authors are grateful to the following private and/or public Italian institutions: (a) AceaPinerolese Spa in Pinerolo (TO) for supplying the SBO sourcing biowastes; (b) Studio Chiono and Associati in Rivarolo Canavese (TO) for making available pilot equipment and services for the production of SBO. Beatriz Soria and Simona Sapino are acknowledged for the TGA in presence of molecular oxygen and DLS measurements, respectively.

Supporting Information Available: TGA derivatives, N_2 adsorption isotherms and BJH mesoporosity analyses, magnetization curves, XPS survey spectra and elements high resolution peaks. This material is available free of charge via the Internet at http://pubs.acs.org.

References

(1) Moreno, J. C.; Gómez, R.; Giraldo, L. Removal of Mn, Fe, Ni and Cu Ions from Wastewater Using Cow Bone Charcoal. *Materials* **2010**, *3*, 452-466.

(2) Wang, Y.; Zhou, D.; Cui Y.; Wang, S.; Chen, Y. Adsorption and Desorption of Cu(II), Zn(II), Pb(II), and Cd(II) on the Soils Amended with Nanoscale Hydroxyapatite. *Environ. Prog. & Sustainable Energy* **2010**, *29*, 233- 241.

(3) Lee, Y.; Elzinga, E. J.; Reeder, R. Sorption Mechanisms of Zinc on Hydroxyapatite: Systematic Uptake Studies and EXAFS Spectroscopy Analysis. *J. Environ. Sci. Technol.* **2005**, *39*, 4042-4048.

(4) Handley-Sidhu, S.; Renshaw, J. C.; Moriyama, S.; Stolpe, B.; Mennan, C.; Bagherias, S.; Yong, P.; Stamboulis, A.; Paterson-Beedle, M.; Sasaki, K.; Pattrick, R. A.; Lead D. J. R.; Macaskie, L. E. Uptake of

Sr^{2+} and Co^{2+} into Biogenic Hydroxyapatite: Implications for Biomineral Ion Exchange Synthesis. *Environ. Sci. Technol.* **2011**, *45*, 6985–6990.

(5) Shekhar, N,; Krishanu, B.; Bikramjit, B. Phase Stability and Microstructure Development in Hydroxyapatite–Mullite System. *Scripta Mater.* **2008**, *58*, 1054–1057.

(6) Wang, D.; Paradelo, M.; Bradford, S. A.; Peijnenburg, W. J. G. M.; Chu, L.; Zhou, D. Facilitated Transport of Cu with Hydroxyapatite Nanoparticles in Saturated Sand: Effects of Solution Ionic Strength and Composition. *Water Res.* **2011,** *45*, 5905-5915.

(7) Pagenkopf, G.; Whitworth, C. Precipitation of Metal-Humate Complexes. *J Inorg. Nucl. Chem.* **1981**, *43*, 1219-1222.

(8) Baigorri, R.; Urrutia, O.; Erro, J.; Mandado, M.; Perez-Juste, I.; Garcia-Mina, J. M. Structural Characterization of Anion-Calcium-Humate Complexes in Phosphate-Based Fertilizers. *ChemSusChem* **2013**, *6*, 1245 – 1251.

(9) Boffa, V.; Perrone, D. G.; Montoneri, E.; Magnacca, G.; Bertinetti, L.; Garlasco, L.; Mendichi, R. A Waste Derived Biosurfactant for the Preparation of Templated Silica Powders. *ChemSusChem* **2010**, *3*, 445 – 452.

(10) Kithva, P. H.; Grøndahl, L.; Kumar, R.; Martin, D.; Trau, M. An Organic Matrix-Mediated Processing Methodology to Fabricate Hydroxyapatite Based Nanostructured Biocomposites. *Nanoscale* **2009**, *1*, 229–232.

(11) Qu, X., Alvarez, P. J. J.; Li, Q. Applications of Nanotechnology in Water and Wastewater Treatment. *Water Res.* **2013**, *47*, 3931–3946.

(12) Iwasaki, T.; Nakatsuka, R.; Murase, K.; Takata, H.; Nakamura, H.; Watano, S. Simple and Rapid Synthesis of Magnetite/Hydroxyapatite Composites for Hyperthermia Treatments Via a Mechanochemical Route. *Int. J. Mol. Sci.* **2013**, *14*, 9365-9378.

(13) Montoneri, E; Boffa, V; Savarino, P; Perrone, D; Ghezzo, M; Montoneri, C; Mendichi, R. Acid Soluble Bio-Organic Substances Isolated from Urban Bio-Waste. Chemical Composition and Properties of Products. *Waste Manage.* **2011**, *31*, 10-7.

(14) Christl, I. Ionic Strength- and pH-Dependence of Calcium Binding by Terrestrial Humic Acids. *Environ. Chem*. **2012**, *9*, 89–96.

(15) Tampieri, A.; D' Alessandro, T.; Sandri, M.; Sprio, S.; Bertinetti, L.; Panseri, S.; Pepponi, G.; Goettlicher, J.; Bañobre-López, M.; Rivas, J. Intrinsic Magnetism and Hyperthermia in Bioactive Fe-Doped Hydroxyapatite. *Acta Biomater*. **2012**, *8*, 843-851.

(16) Panseri, S.; Cunha, C.; D'Alessandro, T.; Sandri, M.; Giavaresi, G.; Marcacci, M.; Hung, C.; Tampieri, A. Intrinsically Superparamagnetic Fe-Hydroxyapatite Nanoparticles Positively Influence Osteoblast-like Cell Behaviour. *J. Nanobiotechnol.* **2012**, *10*:32.

(17) Patterson, A. The Scherrer Formula for X-Ray Particle Size Determination. *Phys. Rev*. **1939**, *56*, 978–982.

(18) Hidmi, L.; Edwards, M. Role of Temperature and pH in $Cu(OH)_2$ Solubility. *Environ. Sci. Technol*. **1999**, *33*, 2607 – 2610.

(19) Kandori, K.; Toshima, S.; Wakamura, M.; Fukusumi, M.; Morisada, Y. Effects of Modification of Calcium Hydroxyapatites by Trivalent Metal Ions on the Protein Adsorption Behavior. *J. Phys. Chem. B* **2010**, *114*, 2399–2404.

(20) Morrissey, R.; Rodríguez-Lorenzo, L. M.; Gross K. A. Influence of Ferrous Iron Incorporation on the Structure of Hydroxyapatite. *J. Mater. Sci.: Mat. Med.* **2005**, *16*, 387-392.

(21) Li, Y.; Nam, C. T.; Ooi, C. P. Iron(III) and Manganese(II) Substituted Hydroxyapatite Nanoparticles: Characterization and Cytotoxicity Analysis. *J. Phys.: Conf. Series* **2009**, *187*, 012024.

(22) Cotescu, A.; Pasuk, I.; Ungureanu, F.; Dinischiotu, A.; Costache, M.; Huneau, F.; Galaup, S.; Le Coustumer, P.; Predoi, D. Physico-Chemical Properties of Nano-sized Hexagonal Hydroxyapatite Powder Synthesized by Sol-Gel. *Dig. J. Nanomater. Bios.* **2010**, *5*, 989 – 1000.

(23) Sing Li, Y.; Church, J. S.; Woodhead, A.L. Infrared and Raman Spectroscopic Studies on Iron Oxide Magnetic Nanoparticles and their Surface Modifications. *J. Magn. Magn. Mater.* **2012**, *324*, 1543–1550.

(24) Lee, W.-H.; Loo, C.-Yee; Van, K. L.; Zavgorodniy, A. V.; Rohanizadeh, R. Modulating Protein Adsorption onto Hydroxyapatite Particles Using Different Amino Acid Treatments. *J. R. Soc. Interf.* **2012**, *9*, 918-927.

(25) Biesinger, M. C.; Payne, B. P.; Grosvenor, A. P.; Laua, L. W. M.; Gerson, A. R.; Smart, R. St. C. Resolving Surface Chemical States in XPS Analysis of First Row Transition Metals, Oxides and Hydroxides: Cr, Mn, Fe, Co and Ni. *Appl. Surf. Sci.* **2011**, *257*, 2717–2730.

(26) Yamashita, T.; Hayes, P. Analysis of XPS Spectra of Fe^{2+} and Fe^{3+} Ions in Oxide Materials. *Appl. Surf. Sci.* **2008**, *254***,** 2441–2449.

(27) Grosseau-Poussard, J. L.; Panicaud, B.; Pedraza, F.; Renault, P. O.; Silvain, J. F. Iron Oxidation Under the Influence of Phosphate Thin Films. *J. Appl. Phys.* **2003**, *94*, 784.

(28) Pratt, A. R. Vivianite Auto-Oxidation. *Phys Chem Miner*. **1997**, *25*, 24–27.

(29) Khachani, M.; Kacimi, M.; Ensuque, A.; Piquemal, J-Y; Connan, C.; Bozon-Verduraz, F., Ziyad M. Iron–Calcium–Hydroxyapatite Catalysts: Iron Speciation and Comparative Performances in Butan-2-ol Conversion and Propane Oxidative Dehydrogenation. *Appl. Catal. A- Gen.* **2010,** *388,* 113–123.

(30) Sun, S.; Zeng H. Size-Controlled Synthesis of Magnetite Nanoparticles. *J. Am. Chem. Soc*. **2002**, *124*, 8204-8205.

(31) Fernane, F.; Mecherri, M. O.; Sharrock, P.; Hadioui, M.; Lounici, H.; Fedoroff M. Sorption of Cadmium and Copper Ions on Natural and Synthetic Hydroxylapatite Particles. *Mat. Charact.* **2008**, *59*, 554 – 559.

(32) Sze, K. F., Lu, Y. J.; Wong, P. K. Removal and Recovery of Copper Ion (Cu^{2+}) from Electroplating Effluent by a Bioreactor Containing Magnetite-Immobilized Cells of Pseudomonas putida 5X. *Resour. Conserv. Recy.* **1996**, *18*, 175-193.

(33) Wong, K. S.; Wong, K. H.; Chung, W. K.; Wong, P. K. Adsorption of Copper Ion on Magnetite-Immobilised Chitin. *Water Sci Technol.* **2007**, *56*, 135-143.

(34) Yamashita, Y.; Jaffe, R. Characterizing the Interactions Between Trace Metal and Dissolved Organic Matter Using Excitation-Emission Matrix and Parallel Factor Analysis. *Environ. Sci. Technol*. **2008**, *42*, 7374–7379.

(35) Senna, M. Determination of Effective Surface Area for the Chemical Reaction of Fine Particulate Materials. *Part. Part. Syst. Char.* **1989**, *6*, 163–167.

(36) Murray, A. R; Kisin, E. R; Tkach, A.V; Yanamala, N.; Mercer, R.; Young, S.H.; Fadeel, B.; Kagan, V. E; Shvedov, A. A. Factoring-in Agglomeration of Carbon Nanotubes and Nanofibers for Better Prediction of their Toxicity versus Asbestos. *Part. Fibre Toxicol.* **2012**, *9*, 10.

(37) De With, G.; Van Dijk, H. J. A.; Hattu, N.; Prijs, K. Preparation, Microstructure and Mechanical Properties of Dense Polycrystalline Hydroxyapatite. *J. Mater. Sci.* **1981**, 16, 1592.

Contents Graphic